

Estimating Bolometric Luminosities of Type 1 Quasars with Self-Organizing Maps

JIE CHEN ^{1,2} LINHUA JIANG ^{1,2} SHENGXIU SUN ^{1,2} ZIJIAN ZHANG ^{1,2} AND MOUYUAN SUN ³

¹*Department of Astronomy, School of Physics, Peking University, Beijing 100871, China*

²*Kauli Institute for Astronomy and Astrophysics, Peking University, Beijing 100871, China*

³*Department of Astronomy, Xiamen University, Xiamen, Fujian 361005, China*

ABSTRACT

We present a new method to calculate bolometric luminosities for unobscured, type 1 quasars with multi-band photometric data. Bolometric luminosity is a fundamental property to understand quasars and it is commonly estimated from monochromatic luminosities using bolometric corrections that often neglect quasar SED diversity. We take advantage of the fact that most quasars now have multi-band observations from UV to mid-IR, and construct SEDs for a well-defined sample of SDSS quasars at $0.5 \leq z \leq 2$. Based on this fiducial sample, we explore quasar SEDs, their diversity, and their relations with bolometric luminosities. We then use unsupervised neural network self-organizing maps (SOM) to describe the SED diversity and compute the bolometric luminosities with a fully-trained SOM model. This method reduces systematical uncertainties compared to the traditional method. In addition, we update the multi-linear regression relations between bolometric luminosity and monochromatic luminosities at restframe 1450 Å, 3000 Å, and 5100 Å. Our method is applicable to large quasar samples with a wide range of luminosity and redshift. We have applied it to the SDSS DR16 quasars. We have also made our code publicly available.

Keywords: Quasars (1319); Surveys (1671); Neural networks (1933); Spectral energy distribution (2129)

1. INTRODUCTION

Quasars show strong radiation across the entire electromagnetic spectrum, powered by the accretion of central supermassive black holes (SMBHs). Their spectral energy distributions (SEDs) reveal the physical properties of the central black hole, accretion disc, dust torus, and possible radio emission. The bolometric luminosity (L_{bol}) of a quasar is defined as the total energy per second over all wavelengths in all directions, and is often computed as the integrated emission of its SED. It is a crucial parameter to understand the SMBH accretion (e.g., Schmidt & Green 1983; Ueda et al. 2003; Volonteri et al. 2003; Hopkins et al. 2007). The bolometric luminosity also represents the mass accretion rate of a SMBH by $L_{\text{bol}} = \eta \dot{M} c^2$, where \dot{M} is the absolute mass accretion rate and η is the accretion efficiency. Combined with the black hole mass (M_{BH}), we can obtain the black hole accretion rate using $\lambda_{\text{Edd}} \equiv L_{\text{bol}}/L_{\text{Edd}}$, where L_{Edd} is the Eddington luminosity. The Eddington ratio is a key parameter that determines the accretion disks geometric structure and dynamical properties (Yuan & Narayan 2014).

Measuring bolometric luminosity presents significant challenges. We summarize the procedure and associated challenges below.

1. First of all, measuring accurate bolometric luminosity requires substantial investment in telescope time to conduct observations across the full wavelength SED.
2. It is controversial whether or how to include radiation in the mid-IR and longer wavelength. Some studies include mid-IR emission from the dust torus (e.g., Elvis et al. 1994; Richards et al. 2006). Others argue that including mid-IR emission would overestimate the total luminosity because it is the reprocessed radiation of the UV/optical photons that is already considered in the SED (e.g., Marconi et al. 2004; Runnoe et al. 2012a; Rosario et al. 2013; Calistro Rivera et al. 2016). In addition, it is unclear how to include radiation in the longer wavelengths that is presumably dominated by the host galaxy.

3. It is difficult to remove the contamination from the host galaxy that contributes more than 30% of the total flux at 5100 Å in low redshift ($z < 0.8$) quasars or AGNs (e.g., Shen et al. 2011; Jalan et al. 2023; Ren et al. 2024). The host fraction depends on luminosity. There are different approaches to estimate the host galaxy contribution. For example, some studies performed a SED fitting to decompose a quasar to an AGN component and a galaxy component (e.g., Lusso et al. 2012; Lyu & Rieke 2017; Duras et al. 2020; Kim et al. 2023). Others used an elliptical galaxy template and one band host galaxy fraction to correct the host galaxy contamination (e.g., Richards et al. 2006; Runnoe et al. 2012a; Krawczyk et al. 2013). Some studies have shown that most low-redshift quasars are in star-forming galaxies (e.g., Rosario et al. 2013; Shanguan et al. 2020; Zhuang et al. 2021).
4. It is challenging to obtain the extreme-UV (EUV) radiation of a quasar. The EUV radiation contributes a large portion of a quasar SED, but it cannot be directly observed because of the absorption by the galactic and extragalactic hydrogen atoms (Lynds 1971). Different studies in the literature often used different models with different EUV SEDs that can affect the bolometric luminosity measurement (Runnoe et al. 2012a; Krawczyk et al. 2013).
5. We often assume that the quasar radiation is isotropic when we calculate the bolometric luminosity. This is apparently not correct. For example, the mid-IR emission from the dust torus is not isotropic, and the optical-UV emission from the accretion disk is highly anisotropic (Stalevski et al. 2016). Hence, an average viewing angle is needed to adjust the bolometric luminosity (e.g., Hubeny et al. 2001; Nemmen & Brotherton 2010; Runnoe et al. 2012a).

Computing the isotropic bolometric luminosity of a quasar with a full wavelength SED is relatively straightforward. It is challenging to obtain bolometric luminosities for large numbers of quasars with photometry in a few bands. Bolometric correction (BC) is a widely used method to estimate bolometric luminosity based on a known monochromatic luminosity. The BC method depends on empirical correlations between the bolometric luminosity and X-ray luminosity (e.g., Brightman et al. 2017; Duras et al. 2020) or continuum luminosities in the UV and optical bands (e.g., Richards et al. 2006; Krawczyk et al. 2013; Runnoe et al. 2012a; Duras et al.

2020). Some studies use the IR luminosity only to compute the bolometric luminosity, assuming that the radiation is almost isotropic (Runnoe et al. 2012b; Kim et al. 2023). In addition, BCs are shown to be luminosity-dependent (e.g., Marconi et al. 2004; Krawczyk et al. 2013; Duras et al. 2020) or Eddington ratio-dependent (e.g., Vasudevan & Fabian 2007; Jin et al. 2012). On the other hand, the diverse SEDs of quasars make it inappropriate to use a simple template to estimate bolometric luminosity (Richards et al. 2006; Auge et al. 2023).

Many quasars now benefit from multi-wavelength observations provided by surveys such as Sloan Digital Sky Survey (SDSS; York et al. 2000), the Galaxy Evolution Explorer (GALEX; Martin et al. 2005), the UK Infra-Red Telescope (UKIRT) Hemisphere Survey (UHS; Dye et al. 2018; Bruursema et al. 2023), the Wide-Field Infrared Survey Explorer (WISE; Wright et al. 2010). These datasets span a wide range of the electromagnetic spectrum, offering a comprehensive view of quasar SEDs. Leveraging this rich multi-band data enables reliable calculation of bolometric luminosities. In principle, incorporating multi-wavelength information would significantly alleviate biases introduced by the luminosity dependency and SED diversity (Su et al. 2025). Despite this fact, current studies still largely rely on the usage of a single monochromatic luminosity and the BC method (e.g., SDSS DR16Q in Wu & Shen 2022).

In this work, we define and calculate isotropic bolometric luminosity under the assumption of an unobscured quasar, $L_{\text{bol}} = \int_0^\infty 4\pi D_L^2 F_\nu d\nu$, where D_L and F_ν are the luminosity distance and rest-frame monochromatic flux. The true anisotropic bolometric luminosity is fL_{bol} , where f is a correction factor. For example, Nemmen & Brotherton (2010) found that f is roughly 0.75. Unless stated otherwise, L_{bol} denotes isotropic luminosity.

We are motivated to improve the isotropic luminosity L_{bol} computation based on multi-band observations rather than a composite SED or single monochromatic luminosity. Quasars that we consider here are typical unobscured type 1 quasars. We mainly use the SDSS-IV quasars from Data Release 16 (DR16Q; Lyke et al. 2020). We collect multi-band observations from the mid-IR to UV for each quasar and use the machine learning algorithm Self-Organizing Map (SOM; Kohonen 1982) to calculate L_{bol} . This method accelerates the calculation of bolometric luminosities and enhances the accuracy by accounting for the correlations between photometric bands. Utilizing multi-band data reduces the systematic uncertainty of bolometric luminosity relative to the single-band BC method. We make the code publicly available.

This paper is formatted as follows. Section 2 introduces our data and quasar sample selection. Section 3 describes the SED construction and the bolometric luminosity calculations. In section 4, we apply the SOM algorithm to our sample to computed bolometric luminosities. Section 5 summarizes the paper. We adopt a cosmology with $H_0 = 70 \text{ km s}^{-1} \text{ Mpc}^{-1}$, $\Omega_M = 0.3$ and $\Omega_\Lambda = 0.7$. The Eddington luminosity is $L_{\text{Edd}} = 1.3 \times 10^{38} (M_{\text{BH}}/M_\odot) \text{ erg s}^{-1}$.

2. DATA AND QUASAR SAMPLE

We use the SDSS-IV quasar catalog from Data Release 16 (DR16Q; Lyke et al. 2020) that contains 750,414 spectroscopically confirmed quasars. Each quasar has photometric data in the five SDSS optical bandpasses (*ugriz*; Fukugita et al. 1996). We use 197,588 relatively bright quasars with $r \leq 20.4$ mag in the redshift range of $0.5 \leq z \leq 2$, after correction for the Galactic extinction. In this redshift range, the *u* and NUV bands cover the peak of the quasar SED in the rest-frame far-UV. We restrict our study to unobscured, type 1 quasars, and quasars are required to have broad Mg II emission lines (2798Å) in the SDSS spectra based on the catalog of Wu & Shen (2022). For each quasar, we retrieve its $E(B-V)$ from the Schlegel et al. (1998) dust map and correct for the Galactic extinction using the extinction coefficients provided by Schlafly & Finkbeiner (2011). We keep quasars with a signal-to-noise ratio (S/N) greater than 5 in all five SDSS bands, and the total quasar number is 193,822.

In order to obtain the photometry of the quasars in other bands, we use the SDSS optical positions to cross-match the quasars with the data from the Galaxy Evolution Explorer (GALEX; Martin et al. 2005), the UKIRT Infrared Deep Sky Survey (UKIDSS; Lawrence et al. 2007), the UK Infra-Red Telescope (UKIRT) Hemisphere Survey (UHS; Dye et al. 2018; Bruursema et al. 2023), Vista Hemisphere Survey (VHS; McMahon et al. 2013), the Wide-Field Infrared Survey Explorer (WISE; Wright et al. 2010). The final sample consists of 79,163 quasars (see details in the following subsections). The Mg II FWHM values of this sample are greater than 4000 km s^{-1} . Figure 1 shows the distributions of the redshifts and monochromatic luminosities L_{2500} (i.e., λL_λ at 2500 Å) for the sample. L_{2500} is calculated by an interpolation from the closest filters. Figure 2 shows the multi-band SEDs of the quasars, and Table 6 in Appendix A provides the multi-band photometry of the sample.

Our quasars are luminous and at redshift about 0.5 to 2. They are point-like sources in ground-based images or GALEX and WISE images. We use total magnitudes or

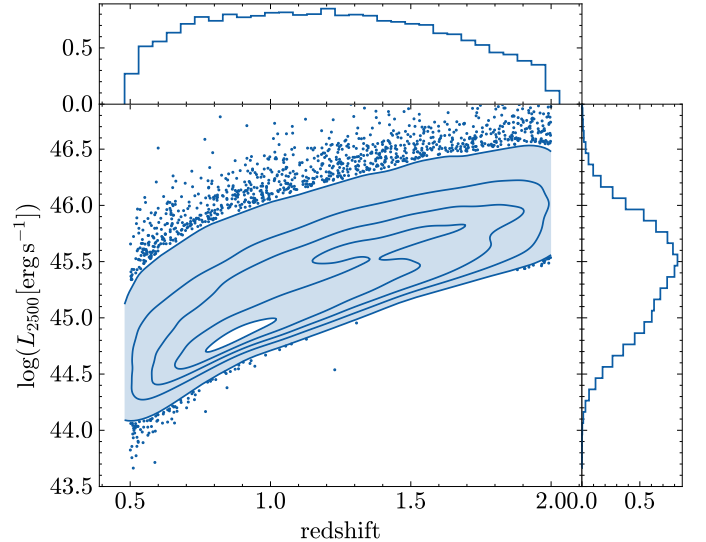


Figure 1. Redshift and L_{2500} distributions of the quasars in our sample. The quasars are represented by the blue contours. The contours indicate 0.005, 0.25, 0.5, 0.75, and 0.95 of the normalized distributions. The histograms of redshift and luminosity are normalized by the total number of the quasars.

total flux to describe them in each band. For SDSS, we use PSFMAG. For other data, we adopt aperture magnitudes with aperture corrections applied (see details in the following subsections).

2.1. Near-IR Data

In the near-IR band, we use the public catalog from UKIDSSDR11PLUS, UHS DR2, and VHS DR6. We crossmatch SDSS DR16Q with these surveys using a radius of $1''$. The survey depths of the UKIDSS Large Area Survey (ULAS) and UKIDSS Galactic Cluster Survey (GCS) in the Y, J, H, and K bands are 20.2 (20.1), 19.6, 18.8, and 18.2 mag (Vega). The UHS is an ongoing UKIRT program that surveys the Northern Hemisphere in the Y, J, H, and K bands. For now, the J and K bands have been publicly available, with a median (5σ) point source sensitivity of 19.6 mag in J and 18.4 mag in K (Vega). Here magnitudes are total magnitudes corrected from aperture magnitudes APERMAG3 within a $2''$ aperture in diameter. The VHS survey observed the southern sky hemisphere in the Y, J, H, and Ks bands, with the depths (5σ) of 20.6, 20.2, 19.2, and 18.2 Vega mag in the four bands. For the overlap regions of ULAS, GCS, and UHS, we use the average photometry from two catalogs. We require that quasars in the final sample should be detected with S/N greater than 5 in at least two near-IR bands. We keep the sources with the flag ERRBITS=0. In total, we have 128,489 matches from the near-IR surveys.

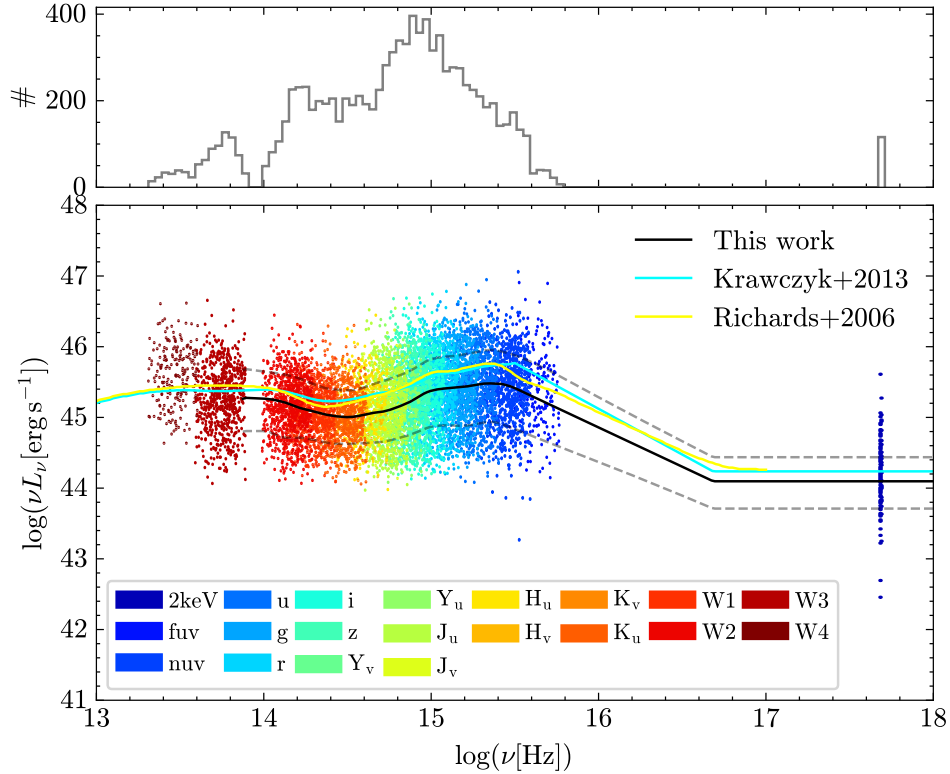


Figure 2. Multi-band SEDs of the quasars in our sample. The upper panel shows the number of SEDs averaged at each frequency. In the lower panel, the solid curve represents the median SED of all quasars in the sample and the dashed curves represent its 1σ ranges. The data points are photometric data of randomly selected 800 quasars.

2.2. Mid-IR Data

We match 128,498 SDSS quasars (with a match length of $1''$) to the AllWISE Data Release (Cutri et al. 2021) to extend their SEDs into the mid-IR range. The WISE bandpasses are generally referred to as W1 through W4, with effective observed frame wavelengths of 3.36, 4.61, 11.82, and 22.13 μm , respectively. We use `w1mpro` to `w4mpro` from ALLWISE, a profile-fit photometry magnitude. We require that all matched quasars have $S/N \geq 5$ in both W1 and W2. If matched quasars have $S/N \geq 3$ in W3 and W4, we also include W3 and W4 in their SEDs. We keep the sources with flag `cc_flag=0` to exclude the contamination and confusion. In total, we have 123,489 matches with AllWISE.

2.3. UV Data

In the UV, we use data from two GALEX bands, FUV (1350-1750 \AA) and NUV (1750-2750 \AA). We start with the sample of 123,498 quasars that satisfy the above IR requirements. We keep quasars only if they have detections in both NUV and FUV bands to avoid an extra scatter in the UV SED. We further require that the positions of the quasars are within the central 0.5-degree radius of the field-of-view (FOV) for any GALEX tiles (Bianchi 2014; Bianchi et al. 2017) to avoid

poor GALEX photometry/astrometry. We then search the GALEX GR6Plus7 catalog for quasar counterparts within a matching radius of $2.6''$ (Trammell et al. 2007). Following a conservative recommendation, sources with artifact flags of 4 or 2 from Bianchi et al. (2017) are removed. For sources detected in multiple tiles, we follow Cai & Wang (2023) and adopt the one with the longest FUV exposure time. We use MAG_AUTO from GALEX, a Kron elliptical aperture magnitude.

In order to correct the Galactic extinction in the GALEX bands, we adopt $A_\lambda/E(B-V)_{\text{SFD}} = 6.783$ and 6.620 for the GALEX FUV and NUV bandpasses, respectively. The correction factors are from Yuan et al. (2013) who used the Fitzpatrick (1999) reddening law with $R_V = 3.1$. We require that the matched quasars should have $S/N \geq 3$ in NUV. Photometry with $S/N \geq 5$ in FUV is included in SED.

The full width at half-maximum of the GALEX point spread function is about $5''$ (Morrissey et al. 2007), so blending and contamination from nearby bright sources are an issue. We check the SDSS images in the GALEX (quasar) positions with a radius of $2.6''$. We exclude 138 quasars that have at least one neighbor brighter than $m_{\text{quasar}} + 1$ mag in the u band.

Our quasar sample spans an FUV brightness range from 17 to 24 mag, which is in the faint regime of the FUV flux nonlinearity calibration (Camarota & Holberg 2014; Wall et al. 2019, 2023). The calibration is based on several white dwarfs to calibrate the nonlinearity for sources brighter than 16 mag. Since our quasars are fainter than the calibration threshold, we assume that no additional correction is required. Finally, we obtain 79,163 matches with GALEX.

2.4. X-Ray Data

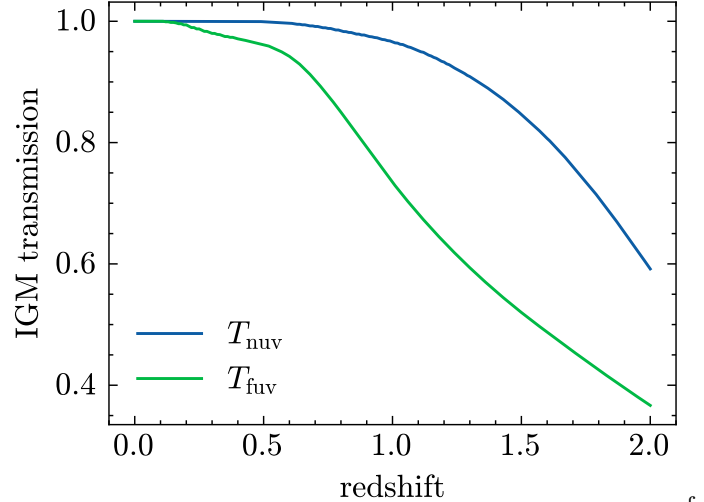
We crossmatch SDSS DR16Q with XMM-Newton Serendipitous Source Catalog (4XMM DR13; Webb et al. 2020; Traulsen et al. 2020), Chandra Source Catalog (CSC v2.1; Evans et al. 2024), and SRG/eROSITA all-sky survey (eRASS DR1; Merloni et al. 2024). For quasars detected in both soft (0.5–1.0 keV for XMM-Newton, 0.2–0.5 keV for eROSITA, and 0.5–1.2 keV for Chandra) and hard (2.0–5.0 keV for XMM-Newton, 1.0–2.0 keV for eROSITA, and 0.5–1.2 keV for Chandra) X-ray bands, we estimate the intrinsic absorption column density using their soft-to-hard band ratios, assuming an intrinsic power-law model modified by the Galactic absorption (HI4PI Collaboration et al. 2016) and intrinsic absorption. The intrinsic power-law photon index Γ is assumed to be 1.7, which is typical for distant X-ray AGNs (e.g., Ranalli et al. 2015). We then calculate the absorption-corrected 2 keV flux. For quasars that are not detected in the hard or soft bands, we assume $\Gamma = 1.7$ and estimate their 2 keV flux using the flux from the nearest detected bands. All X-ray luminosities are corrected for the Galactic absorption. In total, we obtain 11,825 matches with these X-ray surveys in 79,163 quasars.

Due to the limited sky coverage of sensitive X-ray observations, the number of X-ray-detected quasars is significantly lower than those detected in the optical and IR bands. For quasars without X-ray detections (85%), we estimate their X-ray flux using the correlation defined by the $L_{UV} - L_X$ relation based on the luminosities at 2500 Å and 2 keV. Steffen et al. (2006) used 333 quasars with $z \leq 6$ and $\log(\lambda L_\lambda / \text{erg s}^{-1}) > 42$ at 2500 Å and find the following $L_{UV} - L_X$ relation

$$\log(L_{2\text{keV}}) = (0.721 \pm 0.011) \log(L_{2500}) + (4.531 \pm 0.688). \quad (1)$$

We assume an X-ray energy spectral index $\alpha_x = -1$ (photon index $\Gamma = 2$) between 0.2 keV and 10 keV (e.g., George et al. 2000).

3. CONSTRUCTION OF SEDS AND CALCULATION OF BOLOMETRIC LUMINOSITIES



a power law spectrum with an index of -0.44 as a function of redshift in the FUV and NUV bands.

In this section, we first introduce the corrections of the Galactic extinction and the intergalactic medium (IGM; Prochaska et al. 2009) absorption, and construct quasar SEDs. We then calculate bolometric luminosities and estimate bolometric corrections. Finally, we apply multi-band linear regression to improve the accuracy of the bolometric luminosity calculation.

3.1. IGM Absorption Correction

The EUV ($\lambda_{\text{rest}} < 1216 \text{ Å}$) part of the quasar spectrum is significantly attenuated by the IGM. To statistically correct the IGM absorption, we model the IGM transmission as a result of absorption by both Lyman continuum (LyC) and Lyman series lines (LyL) following Cai & Wang (2023). The total IGM transmission is $T_\lambda = \exp(-\tau_{\text{eff}})$, where the total effective optical depth, $\tau_{\text{eff}} = \tau_{\text{eff}}^{\text{LyC}} + \tau_{\text{eff}}^{\text{LyL}}$, with the effective LyC optical depth, $\tau_{\text{eff}}^{\text{LyC}}$, and the effective LyL optical depth, $\tau_{\text{eff}}^{\text{LyL}}$. The optical depth models the average attenuation of a source assuming Poisson-distributed neutral hydrogen (HI) clouds along the line of sight. Adopting the Faucher-Giguère (2020) distribution of absorbers with the HI column density of $12 \leq \log N_{\text{HI}} \leq 22$ and the Doppler broadening parameter of $b = 30 \text{ km s}^{-1}$, we calculate the average IGM transmission curves for redshift from 0.5 to 2, with a step size of 0.01. We assume a power-law continuum with an index from the continuum fitting in Wu & Shen (2022), and compute its filter-weighted broadband mean IGM transmission to correct the photometry in the FUV and NUV bands. Figure 3.1 shows an example of the mean broadband IGM transmission with an index of -0.44 for the two bands at each redshift (Vanden Berk et al. 2001).

3.2. Median SED and SED Diversity

To illustrate the diversity of type 1 quasar SEDs, we first build a median quasar SED. To construct quasar SEDs, we convert their flux densities to luminosities and shift the bandpasses to the rest frame. All fluxes here are energy-weighted in SEDs. Figure 2 shows the SEDs of 800 randomly selected quasars from our samples. The Galactic extinction and IGM absorption have been corrected. We then create a data grid with a step size of 0.02 in log frequency, and linearly interpolate the quasars SEDs to match the grid. To generate the median energy distribution, we take a median value in $\log \nu L_\nu$ of all the data in each frequency bin, and it is shown as the black solid curve in Figure 2. We use the 16th and 84th percentiles of the SEDs as the 1σ confidence level (i.e., the dashed line in the figure). The host galaxy contribution has not been removed in this step. For comparison, the mean quasar SEDs from Richards et al. (2006) and Krawczyk et al. (2013) are shown in yellow and cyan, respectively. Our sample is slightly fainter, and thus our median SED is relatively low. We also try a brighter quasar sample with $r \leq 19.1$ mag, and find that the median SED is consistent with those from Richards et al. (2006) and Krawczyk et al. (2013).

Figure 3 shows the diversity of the quasar SEDs in the UV to IR range. In this figure, we display 4000 randomly selected quasars from our sample and their SEDs are normalized at 5100 Å. These 4000 UV-IR SEDs follow the same L_{5100} distribution of the whole sample. The large scatter suggests a highly diverse nature of quasar SEDs that cannot be well explained by a single quasar template. Note that the y -axis is on a logarithmic scale that has reduced the scatter visually. The reason for the SED diversity is the combination of many factors, including host galaxy contributions, black hole masses, accretion rates, viewing angles, etc. The details are beyond the scope of this study.

3.3. Host Galaxy Correction

Previous studies have found empirical anti-relations between the quasar host galaxy fraction and luminosity or redshift, but the scatters of these relations are typically very large (e.g., Shen et al. 2011; Jalan et al. 2023; Ren et al. 2024). Here we use the relation between the host fraction and luminosity at 5100 Å from Jalan et al. (2023). Some studies have shown that most low-redshift quasars are in star-forming galaxies (e.g., Rosario et al. 2013; Shangguan et al. 2020; Zhuang et al. 2021). Hence, we use the spiral galaxy template of Assef et al. (2010) to represent the host galaxy. Compared to elliptical galaxies, spiral galaxies have a larger short-wavelength contribution from the star-forming component. Removing

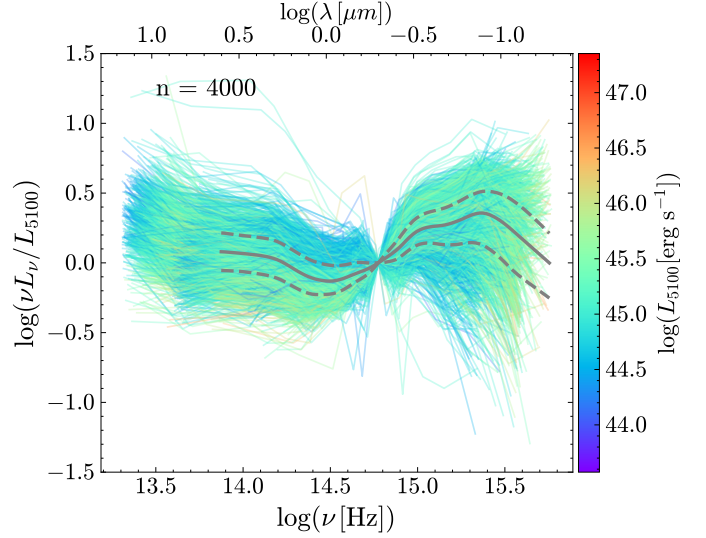


Figure 3. Diversity of quasar SEDs. The color-coded curves represent 4000 randomly selected quasars from our sample. The SEDs have been normalized at 5100 Å. The gray solid curve is the median normalized SED with 1σ level indicated by the dashed curves.

galaxy components decreases the bolometric luminosity by an average of 0.05 dex. In the near future, the China Space Station Telescope and Euclid surveys will cover nearly half the sky in the wavelength range from NUV to near-IR, which will allow us to estimate host components for individual quasars by image decomposition.

3.4. Emission Line Correction

We calculate the K-correction of the broadband photometry for individual sources based on the continuum fitting results by Wu & Shen (2022). Due to the fixed wavelength coverage in the observed frame, the SDSS spectra do not cover some strong lines (e.g., Ly α , C IV) for quasars in some particular redshift ranges, but they cover Mg II for all our quasars. Therefore, we use the empirical relation of equivalent width between Mg II and other lines (i.g., Ly α , C IV, H β , and H α lines). We artificially add the lines in the extrapolated continuum and compute the corresponding K-correction from UV to near-IR. After the correction of the line emission, the bolometric luminosity decreases by about 0.02 dex on average.

3.5. Bolometric Luminosity Measurement and Wavelength Range Selection

Bolometric luminosity is the integrated area under the SED curve. Its mathematical definition is as follows,

$$L_{\text{bol}} = \int_0^\infty L_\nu d\nu = \int_{-\infty}^\infty \ln(10) \nu L_\nu d \log(\nu). \quad (2)$$

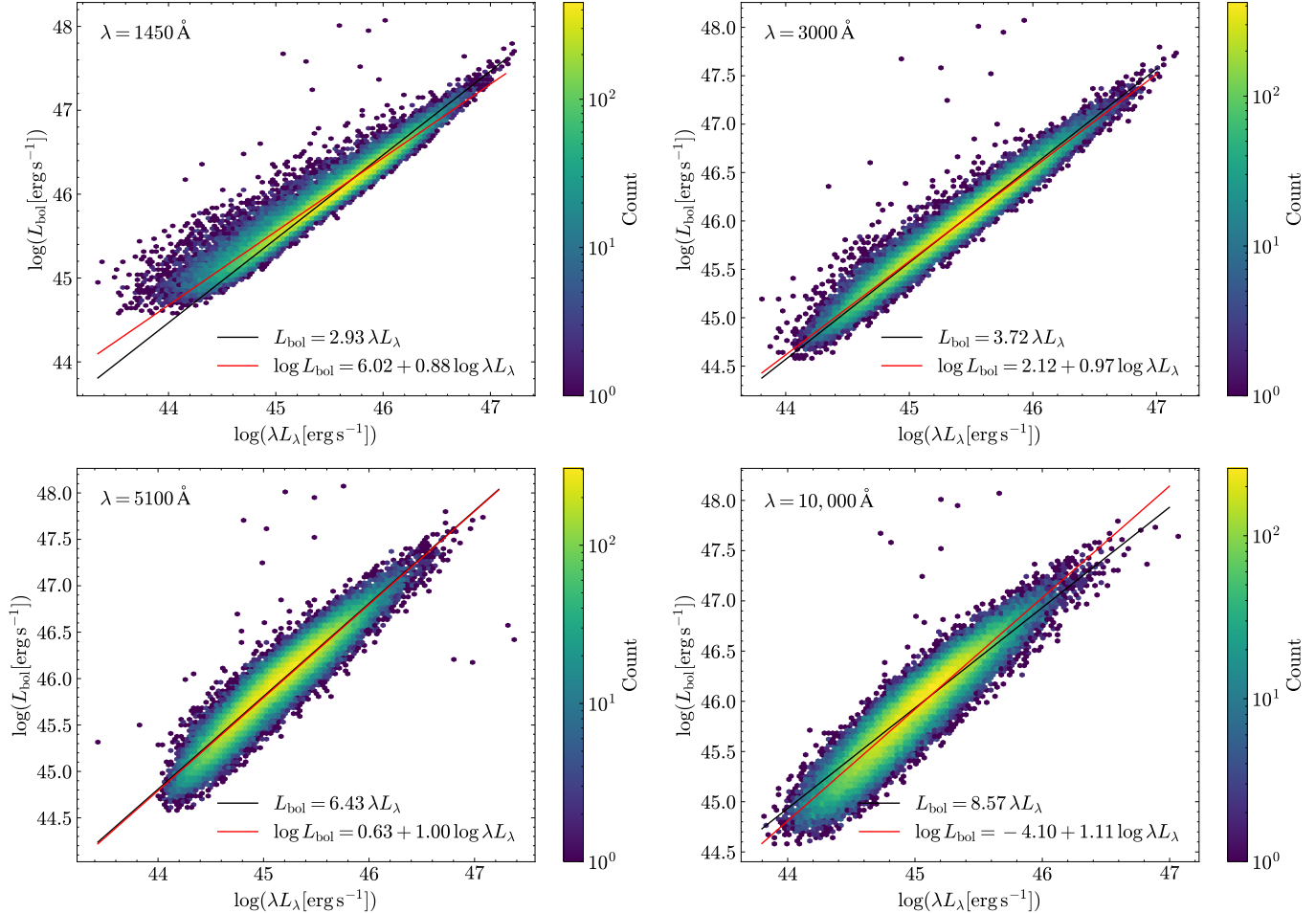


Figure 4. Relation between bolometric luminosity and monochromatic luminosity at 1450 Å, 3000 Å, 5100 Å, and 10,000 Å. The black lines indicate the BC fitting and the red lines show the linear regression.

In practice, the observed wavelengths are limited. The choice of the integration range is an unclear issue as we discussed in the Introduction. Regarding the IR SED, some previous studies suggested that IR emission should not be included because it represents the reprocessed radiation of accretion disc photons by dusty torus (e.g., Marconi et al. 2004). There is a similar claim for the X-ray emission. Hard X-ray emission is generated through the inverse-Compton upscattering of disc photons by electrons in a hot corona. The reprocessing of these photons depends on the geometry of the corona (Sobolewska et al. 2004a,b). Therefore, the definition of the wavelength range for the bolometric luminosity computation is contingent upon the understanding of the structure surrounding the SMBH.

Our approach is to make the wavelength range flexible (e.g., Krawczyk et al. 2013). We use an integration range of 4 μ m-10 keV (default range) in this paper. On the other hand, our code allows users to choose a different range for their own scientific purposes. About 20% of our rest-frame SEDs do not reach 4 μ m because of the

low detection rate in W3 and W4. We use KNNImputer (Troyanskaya et al. 2001), an imputation for completing missing values using k-Nearest Neighbors, to recover the missing SEDs with $n_neighbors = 100$ in our samples. The bolometric luminosities of full-coverage samples are calculated based on recovering SEDs. Conclusions for the paper remain quantitatively consistent when excluding these samples.

Calculating the uncertainty of bolometric luminosity is also challenging. Many sources of uncertainty exist, including but not limited to the SED interpolation, SED variation, host galaxy correction, orientation, etc. In this work, we do not consider these issues in detail except for the uncertainty from the interpolation. We emphasize that the uncertainty of bolometric luminosity is underestimated in this work and most other works.

3.6. Isotropy and Viewing Angles

One popular model to describe the SMBH gas accretion in AGNs is the geometrically thin but optically thick disk (e.g., Novikov & Thorne 1973; Shakura &

Sunyaev 1976). A face-on accretion disc is usually UV-brighter than an edge-on disc, so bolometric corrections based on face-on observations may overestimate bolometric luminosities. Based on studies of the theoretically thin accretion disc models, Runnoe et al. (2012a) suggested a correction to bolometric luminosities with the assumption of isotropy. Using a randomly selected quasar sample from Shang et al. (2011) and a preferential view angle of 31° from Barthel (1989), Nemmen & Brotherton (2010) suggested bolometric correction factor f as 0.75. This correction will increase the bolometric luminosity value. We add this correction as an option in the final code.

3.7. Bolometric Correction and Multi-band Linear Regression

Bolometric correction (BC) is a widely used method to calculate bolometric luminosities for large quasar samples. This traditional BC is given as

$$\text{BC}_\nu = \frac{L_{\text{bol}}}{\nu L_\nu}. \quad (3)$$

This definition assumes a coefficient of unit between monochromatic luminosity and bolometric luminosity in the logarithmic space. Bolometric correction values from different works are usually different. Table 1 summarizes correction values from previous studies, as well as our correction values. The selection of the X-ray wavelength boundaries has little influence on the calculation of the bolometric luminosity, because the X-ray luminosity is approximately one order of magnitude lower than the UV/optical luminosity. We can see that the BC values highly rely on the IR wavelength used for the computation, since the IR emission contributes a large portion of the whole quasar SED.

Nemmen & Brotherton (2010) and Runnoe et al. (2012a) found that the relation between monochromatic luminosity and bolometric luminosity depends on luminosity, and thus used a linear relationship in the logarithmic space. In Figure 4, we show the relation between bolometric luminosity and monochromatic luminosity at 1450 Å, 3000 Å, 5100 Å, and 10,000 Å for our sample. We evaluate the bolometric correction as a function of bolometric luminosity in Figure 5. The horizontal dashed lines represent the median BC values for the corresponding wavelengths. The figure clearly displays a luminosity dependence with a large scatter. Specifically, the optical and IR BCs overestimate L_{bol} at low luminosities and underestimate L_{bol} at high luminosities, while the UV BCs show an opposite trend.

To take advantage of the multi-band data, we use the least square method to fit the relationship between bolometric luminosity and monochromatic luminosity at four

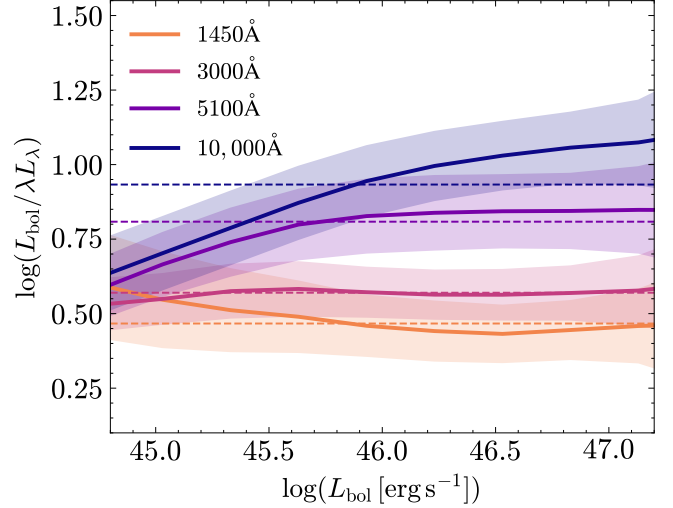


Figure 5. Bolometric correction as a function of bolometric luminosity. The dashed horizontal lines represent the median values of the bolometric corrections.

wavelengths, i.e., 1450 Å, 3000 Å, 5100 Å, and 10,000 Å. We optimize the multiple linear regression (MLR) by minimizing χ^2 , given by $\chi^2 = \sum (y_i - y_{i,\text{model}})^2 / (\sigma_{y,i}^2)$, where y_i , $y_{i,\text{model}}$, and $\sigma_{y,i}$ are $\log(L_{\text{bol}})$, the model $\log(L_{\text{bol}})$, and the 1σ uncertainty of y_i , respectively. Table 2 shows the multiple linear regression results from one monochromatic luminosity. Table 3 shows the multiple linear regression results from two and three monochromatic luminosities. The uncertainties of the slope and intercept are calculated following Hogg et al. (2010) assuming a normal distribution for the computed bolometric luminosities. For each BC, we calculate a fractional residual $f = (L_{\text{bol,model}} - L_{\text{bol,true}}) / L_{\text{bol,true}}$ between the predicted bolometric luminosity and the true value. The dispersion of the fractional residual (σ_f) represents the accuracy of the bolometric luminosity computation. The σ_f is estimated as half the difference between the 16th and 84th percentiles of the fractional residual. The σ_f values based on one, two, and three monochromatic luminosities are about 24.5%, 16.7%, and 13.6%, respectively.

We also compare monochromatic luminosities with spectra-based luminosities from Wu & Shen (2022). These monochromatic luminosities are roughly the same with a large scatter in the low luminosity range likely due to quasar variability and fiber loss. We perform a test and replace the *ugriz* photometry with the SDSS spectra, and find a small difference (1%) in bolometric luminosity with a 7% scatter. The bolometric corrections from spectral-photometric combined bolometric luminosity have a larger σ_f of 26% than that inferred from broadband SED.

Table 1. Bolometric corrections and comparison with previous results

	This paper	This paper	Richards et al. (2006)	Runnoe et al. (2012a)	Krawczyk et al. (2013)
Integration range	4 μ m-10 keV	1 μ m-10 keV	30 μ m-10 keV	1 μ m-8 keV	1 μ m-2 keV
BC ₁₄₅₀	2.93 \pm 0.64	2.27 \pm 0.39	(2.33 ^a)	4.2 \pm 0.1	...
BC ₃₀₀₀	3.72 \pm 0.68	2.86 \pm 0.63	5.62 \pm 1.14	5.2 \pm 0.2	BC ₂₅₀₀ = 2.75 \pm 0.40
BC ₅₁₀₀	6.43 \pm 1.84	4.98 \pm 1.73	10.3 \pm 2.1	8.1 \pm 0.4	4.33 \pm 1.29 (7.79 \pm 1.69 ^b)
log(L_{bol}) range	44.58-48.07	-	45.06-47.43	45.13-47.30	45.06-47.43

^avalue for the mean SED of all quasars in Richards et al. (2006) integrating from 1 μ m to 8 keV as reported by Runnoe et al. (2012a).

^bvalue with integrating from 30 μ m to 10 keV as reported by Krawczyk et al. (2013).

Table 2. Bolometric corrections from one monochromatic luminosity.

Wavelength	$L_{\text{bol}} = \text{BC}_\lambda \lambda L_\lambda$	f	σ_f
1450 Å	$L_{\text{bol}} = (2.93 \pm 0.64) \lambda L_\lambda$	0.000	0.203
3000 Å	$L_{\text{bol}} = (3.72 \pm 0.68) \lambda L_\lambda$	0.000	0.180
5100 Å	$L_{\text{bol}} = (6.43 \pm 1.84) \lambda L_\lambda$	0.000	0.290
10,000 Å	$L_{\text{bol}} = (8.57 \pm 2.91) \lambda L_\lambda$	0.000	0.359
Wavelength	$\log(L_{\text{bol}}) = A + B \log(\lambda L_\lambda)$	f	σ_f
1450 Å	$\log(L_{\text{bol}}) = (6.020 \pm 0.001) + (0.879 \pm 0.001) \log(\lambda L_\lambda)$	0.068	0.197
3000 Å	$\log(L_{\text{bol}}) = (2.118 \pm 0.001) + (0.966 \pm 0.01) \log(\lambda L_\lambda)$	-0.002	0.176
5100 Å	$\log(L_{\text{bol}}) = (0.633 \pm 0.001) + (1.004 \pm 0.001) \log(\lambda L_\lambda)$	-0.028	0.282
10,000 Å	$\log(L_{\text{bol}}) = (-4.101 \pm 0.001) + (1.112 \pm 0.001) \log(\lambda L_\lambda)$	-0.018	0.323

NOTE—Uncertainties for all fits in this table are 1 σ confidence level.

Table 3. Bolometric corrections from two and three monochromatic luminosities.

Two-Wavelength	$\log(L_{\text{bol}}) = A + B_1 \log(\lambda_1 L_1) + B_2 \log(\lambda_2 L_2)$				f	σ_{f}
1450 Å, 3000 Å	$A = 4.139 \pm 0.001$	$B_1 = 0.238 \pm 0.001$	$B_2 = 0.684 \pm 0.001$		0.020	0.145
1450 Å, 5100 Å	$A = 3.018 \pm 0.001$	$B_1 = 0.441 \pm 0.001$	$B_2 = 0.508 \pm 0.001$		0.014	0.140
1450 Å, 10,000 Å	$A = 0.571 \pm 0.001$	$B_1 = 0.489 \pm 0.001$	$B_2 = 0.515 \pm 0.001$		0.019	0.136
3000 Å, 5100 Å	$A = 3.199 \pm 0.001$	$B_1 = 0.804 \pm 0.001$	$B_2 = 0.140 \pm 0.001$		0.004	0.167
3000 Å, 10,000 Å	$A = 1.902 \pm 0.001$	$B_1 = 0.766 \pm 0.001$	$B_2 = 0.208 \pm 0.001$		0.004	0.162
5100 Å, 10,000 Å	$A = 0.727 \pm 0.001$	$B_1 = 0.757 \pm 0.001$	$B_2 = 0.246 \pm 0.001$		−0.013	0.254
Three-Wavelength	$\log(L_{\text{bol}}) = A + B_1 \log(\lambda_1 L_1) + B_2 \log(\lambda_2 L_2) + B_3 \log(\lambda_3 L_3)$				f	σ_{f}
1450 Å, 3000 Å, 5100 Å	$A = 3.159 \pm 0.001$	$B_1 = 0.342 \pm 0.001$	$B_2 = 0.254 \pm 0.001$	$B_3 = 0.350 \pm 0.001$	0.013	0.132
1450 Å, 3000 Å, 10,000 Å	$A = 1.288 \pm 0.001$	$B_1 = 0.351 \pm 0.001$	$B_2 = 0.276 \pm 0.001$	$B_3 = 0.360 \pm 0.001$	0.017	0.121
1450 Å, 5100 Å, 10,000 Å	$A = 1.215 \pm 0.001$	$B_1 = 0.451 \pm 0.001$	$B_2 = 0.211 \pm 0.001$	$B_3 = 0.328 \pm 0.001$	0.016	0.128
3000 Å, 5100 Å, 10,000 Å	$A = 1.749 \pm 0.001$	$B_1 = 0.807 \pm 0.001$	$B_2 = -0.092 \pm 0.001$	$B_3 = 0.262 \pm 0.001$	0.006	0.162

NOTE—Uncertainties for all fits in this table are 1 σ confidence level.

4. RESULTS

Machine learning (ML) emerges as a transformative tool for multi-dimensional datasets. Combining the strength of photometric surveys with the advanced machine learning tool may offer a pathway to overcome the challenge of calculating robust bolometric luminosities for large numbers of quasars. By learning directly from the data, ML techniques can efficiently process multi-dimensional datasets and uncover complex patterns that are otherwise difficult to model with traditional approaches (Ball & Brunner 2010; Acquaviva 2016; Baron 2019). The Self-Organizing Map (SOM; Kohonen 1982) is an unsupervised ML algorithm that projects high-dimensional data onto a 2D map that nevertheless preserves the topology. SOM has been widely applied in astrophysics. For instance, Hemmati et al. (2019) and La Torre et al. (2024) applied SOM to improve photometric redshift estimation for large-scale galaxy surveys. La Torre & Pacucci (2024) used SOM to constrain the properties of slowly accreting black holes. These studies underscore the flexibility of SOM in addressing complex, high-dimensional challenges in astrophysical researches.

SOM maps a high-dimensional parameter space onto a 2D lattice, where each neuron is associated with a weight vector corresponding to the high-dimensional input space. Here, we use the Python library SomPY¹ (Moosavi et al. 2014) to construct and train our SOM model. In SomPY, training data are normalized to the unit variance with a zero mean. The training of a SOM begins with initializing the weight vectors using the principal component analysis (PCA; Chatfield & Collins 1980), followed by the iterative adjustment of weights. For each data point in the training set, the Best Matching Unit (BMU), the neuron whose weight vector is closest to the input, is identified using a Euclidean distance metric. The BMU's weight vector is updated to move closer to the input data, and a neighborhood function ensures that adjacent neurons in the lattice are similarly adjusted. This iterative process continues until a convergence occurs when the weights stabilize. As an unsupervised method, SOM does not require labeled input data, making it particularly valuable for exploratory data analysis and visualization. We refer to the neuron as a ‘cell’ in a 2D map in the following context.

4.1. Generating SOM

In this work, the input parameter space has 11 dimensions representing the rest-frame quasar SEDs (i.e., 11 monochromatic luminosities). We select monochro-

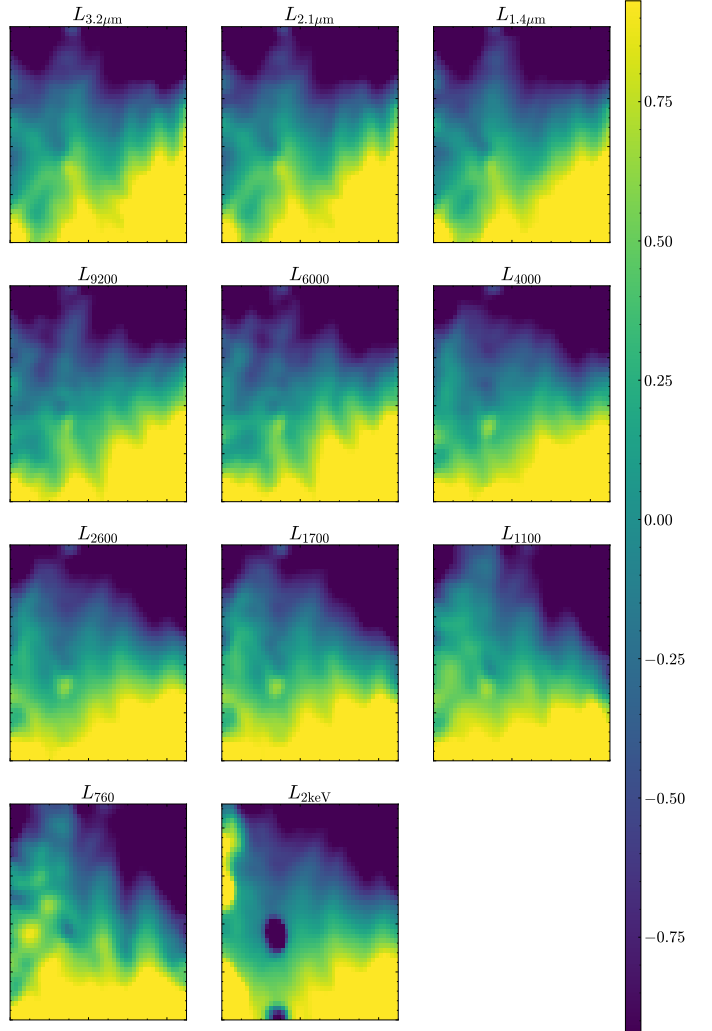


Figure 6. Distribution of 11 normalized monochromatic luminosities on the 45×45 trained SOM.

matic luminosities in the range of $3.2 \mu\text{m}$ to 760 \AA , along with the 2 keV luminosity. Our photometric data are available for most quasars in this wavelength range. To evaluate the precision and adaptability of this method, we randomly split our sample into a training set (80%) and a test set (20%).

The SOM performance depends on the map size and geometry (see Davidzon et al. 2019). The map size and geometry should balance a good sampling of the data and a high resolution. A sample rate is defined as the fraction of the cell with more than 20 samples. The quantization error is the mean of the Euclidean distances of all training data to their BMUs. A smaller quantization error indicates a high resolution. We choose a 45×45 SOM with a sampling rate of 90% and a quantization error of 0.11. Figure 6 shows the distribution of 11 normalized monochromatic luminosities on the 45×45 map. We also verify that the 11 monochromatic lumi-

¹ <https://github.com/sevamoo/SOMPY>

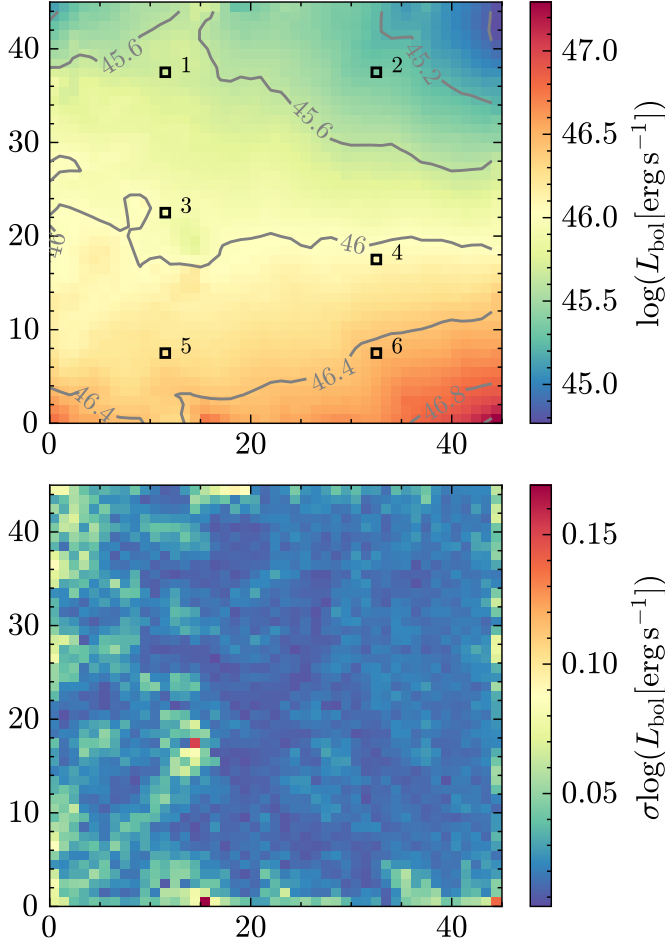


Figure 7. Upper panel: SOM with cells color-coded by the median values of $\log(L_{\text{bol}})$. The gray contours represent the levels of the $\log(L_{\text{bol}})$ values. The open black squares represent six cells: Cell 1 = [33, 38], Cell 2 = [12, 38], Cell 3 = [12, 23], Cell 4 = [33, 18], Cell 5 = [12, 8], Cell 6 = [33, 8]. Lower panel: SOM with cells color-coded with the 1σ level of $\log(L_{\text{bol}})$.

nosity distributions in the input dataset and across the SOM cells are consistent, ensuring that the trained SOM represents the input data.

4.2. Bolometric Luminosity Projection

Since bolometric luminosity depends on the SED, objects in the same cell share similar SEDs and bolometric luminosities. We compute the median value and 1σ deviation (i.e., half the difference between the 84th and 16th percentiles) of $\log(L_{\text{bol}})$ for each cell. Figure 7 shows the trained SOM color-coded by the median and 1σ deviation of $\log(L_{\text{bol}})$. The $\log(L_{\text{bol}})$ values smoothly increase nearly vertically from top to bottom, and the $\sigma(\log L_{\text{bol}})$ values are globally small, indicating that this SOM model is a good classifier for $\log(L_{\text{bol}})$. To demonstrate that this SOM describes the SED diversity, we

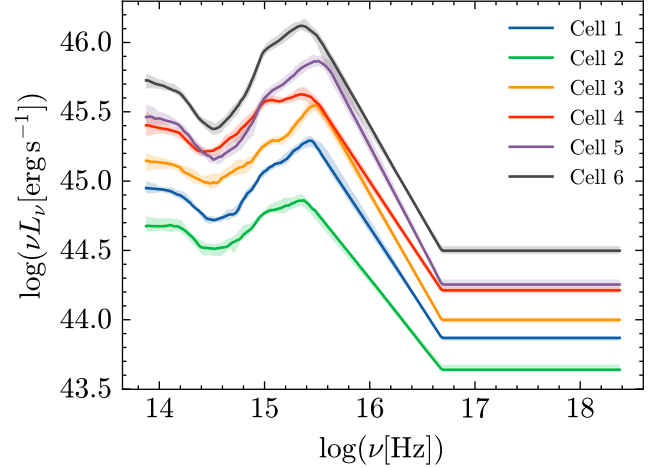


Figure 8. Six median quasar SEDs (solid curves) with 1σ dispersions (shaded area) from six cells, i.e., the black open circles in Figure 7.

select six SEDs from six cells representing different luminosities in Figure 8. The shaded region is the 1σ deviation of the SEDs, suggesting that the SEDs in each cell are well constrained, with small deviations around the median.

Figure 9 compares the true values with the SOM-derived values for $\log(L_{\text{bol}})$ in the training and test samples. We also compute four statistical parameters, including the normalized median absolute deviation (σ_{NMAD}), outlier fraction η , root mean squared error (RMSE), and bias. The outlier fraction η is the fraction with $|\log(L_{\text{bol,true}}) - \log(L_{\text{bol,som}})| \geq 2\sigma$, where σ is the standard deviation of the $\log(L_{\text{bol,true}}) - \log(L_{\text{bol,som}})$ values. With the SOM model, the $\log(L_{\text{bol}})$ estimation is accurate in the training and test samples, with $\sigma_{\text{NMAD}} \approx 0.02$ and $\text{RMSE} \approx 0.03$. We also use the target selection flags from SDSS DR16Q and separate WISE-selected quasars or X-ray-selected quasars as a test sample. The remaining quasars stay in the training sample. Overall, σ_{NMAD} and RMSE are largely unaffected by sample selection. For each quasar, we use the systematic uncertainty, i.e., the dispersion of $\log(L_{\text{bol}})$ within the best-fit cell.

We project other fundamental AGN parameters (black hole mass and Eddington ratio) in the SED-based SOM model. They have worse correlations with the SED compared to the bolometric luminosity. It is likely due to large uncertainties in the current estimate of single-epoch black hole masses, or an intrinsic weak correlation with SED (Duras et al. 2020).

4.3. Comparing with the Bolometric Correction Method

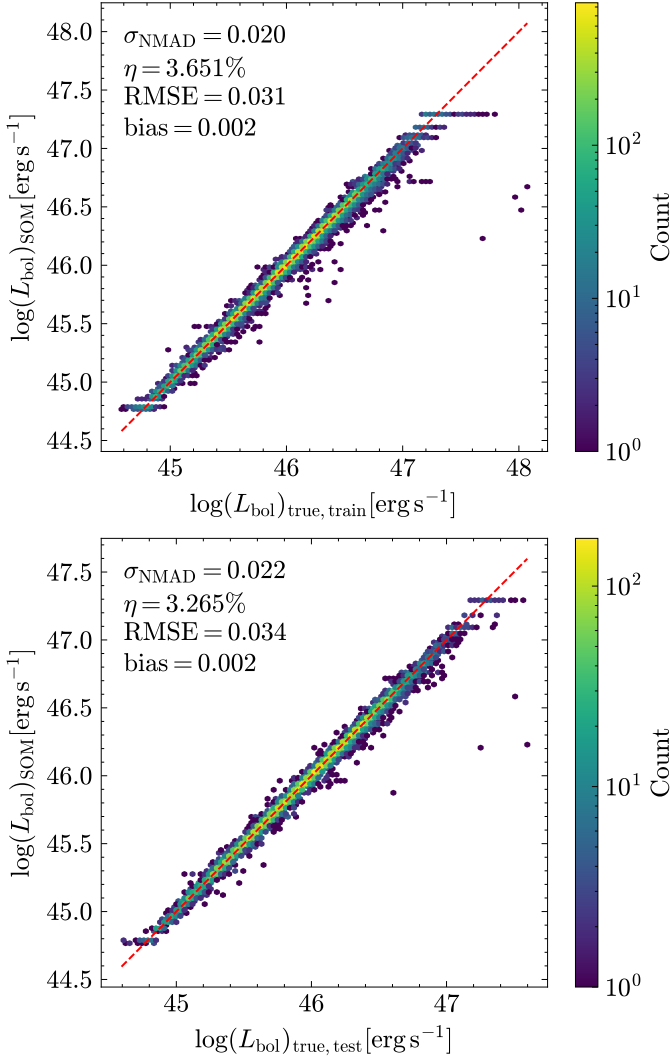


Figure 9. Comparison between the true $\log(L_{\text{bol}})$ and SOM-derived $\log(L_{\text{bol}})$ values in the training and test sets. The red line is the one-to-one line.

We calculate the median and dispersion of fractional residuals between the SOM-derived bolometric luminosity and the true value. For comparison, we also use the BCs and linear relations with monochromatic luminosities to predict bolometric luminosities. The distributions of the fractional residuals from different methods are shown in Figure 10, where the SOM method result is from all samples. The line in the box represents the median, while the top and bottom edges correspond to the 75th and 25th percentiles. The whiskers extend to the minimum and maximum values. The median values of the fractional residuals are near zero in all methods. The SOM method with 11 monochromatic luminosities has the smallest dispersion relative to other methods, with σ_f of 4.9%. For the method with BC, σ_f is about 20.3%, 18.0%, and 29.0% at 1450 Å, 3000 Å, and 5100 Å,

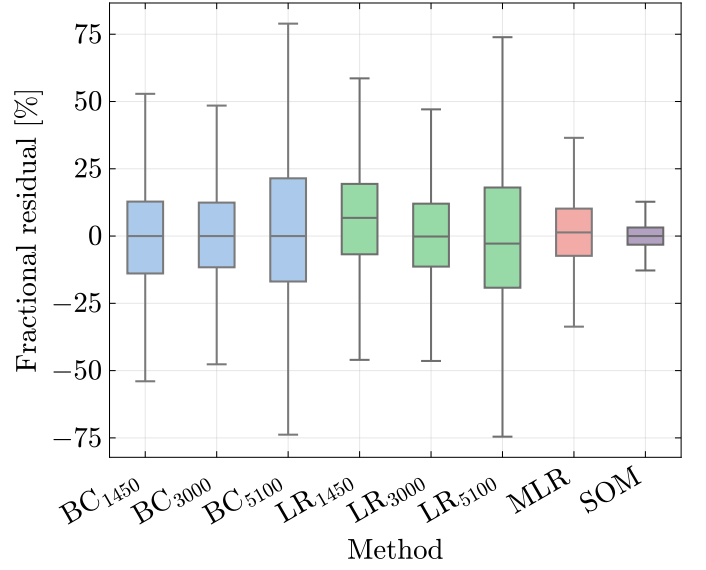


Figure 10. Fractional residuals from different methods, including BCs at 1450 Å, 3000 Å, and 5100 Å, linear regression with monochromatic luminosities at 1450 Å, 3000 Å, and 5100 Å, multiple linear regression with monochromatic luminosities at 1450 Å, 3000 Å, and 5100 Å, and the SOM method. For clarity, outliers are not shown.

respectively. For the method of the linear fitting with monochromatic luminosity, σ_f is about 19.7%, 17.6%, and 28.2% at 1450 Å, 3000 Å, and 5100 Å, respectively. In short, the SOM method with 11 monochromatic luminosities has largely reduced the dispersion of the fractional residual.

4.4. Handling Limited Data

We also use the SOM model to compute the bolometric luminosities of quasars with limited data. As we mentioned earlier, large-area surveys such as SDSS, UKIDSS, and WISE covered most of the currently known quasars, so these quasars have photometric data from UV to mid-IR. Despite the fact, many quasars have fewer photometric data points available. Therefore, we explore how to use SOM to deal with limited data. La Torre et al. (2024) proposed a method to recover specific missing information by randomly drawing 5000 new values of the missing feature from the distribution of the rest of the training sample, under the assumption that the missing value obeys the same distribution as the training sample. Given the new set of input features, they created a 2D likelihood surface of possible cells and extracted the probability distribution function of the interested property. Since the features in SEDs are highly correlated, randomly drawing new values may produce non-physical SEDs. Hence, we use KNNImputer (Troyanskaya et al. 2001), an imputation for completing miss-

Table 4. Effect of bolometric luminosity recovery for different missing bands

Limited SED	f	σ_f
All bands (all sample)	0.000	0.049
All bands (training set)	0.000	0.048
All bands (test set)	0.001	0.052
NUV-IR (8 bands)	0.001	0.129
NUV-NIR (5 bands)	-0.005	0.137
NUV-optical (4 bands)	-0.008	0.143
u-IR (7 bands)	-0.010	0.159
u-NIR (5 bands)	-0.014	0.160

ing values using k-Nearest Neighbors, to recover missing data. Each sample’s missing values are imputed using the mean value of the nearest n neighbors found in the training set. We set $n_neighbors = 100$ in `KNNImputer`. After recovering limited SEDs, we use the fully-trained SOM model to compute bolometric luminosities.

We use the test sample as an example to demonstrate the capability of `KNNImputer`. We select five typical limited SEDs that mimic the absence of real observations. These consecutive SEDs are divided into two categories, where SEDs start from 1700 Å and 2600 Å, respectively. Table 4 lists the details, including the number of photometric data points. Figure 11 shows an example of applying `KNNImputer` to recover limited SEDs. The fractional residuals after recovering limited SEDs are shown in Figure 12. Compared with fractional residuals using all bands above, a limited SED has a higher fractional residual, because less information introduces a larger uncertainty. The results also indicate that the UV part of the SED is important to reduce estimator uncertainties. We also test limited SEDs without recovery and find that the closest BMU ignores the missing features. The 1σ confidence level of the fractional residual increases about 5% for the five limited SEDs, suggesting that recovery is necessary.

4.5. Application to SDSS DR16Q

We apply our method to the remaining quasars in the SDSS DR16Q sample and calculate their $\log(L_{\text{bol}})$. We focus on typical type 1 luminous quasars with $\log(L_{2500}/\text{erg s}^{-1}) > 43.7$ at $z < 5$ and obtain 633,373 sources. We crossmatch with the existing surveys to obtain photometric data across UV to near-IR following the same method in section 2. For W1 and W2 in the mid-IR, we use `unWISE` (Schlafly et al. 2019) to increase the detection rate. For the IGM absorption correction, we use the average IGM transmission curves for FUV, NUV, u , g , and r bands for redshift from 0 to 5. Then we constructed restframe SEDs with photometric points

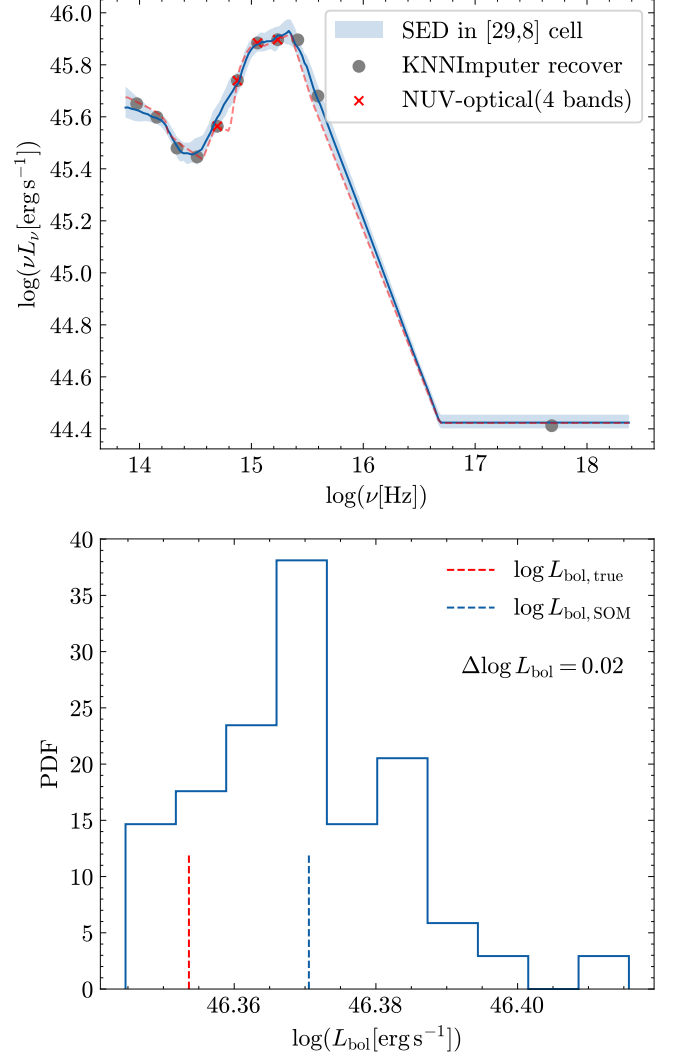


Figure 11. An example for `KNNImputer` to recover limited SEDs. The upper panel shows input and recovered SEDs. The input data only contains 4 band luminosities from NUV to optical (red crosses). The gray dots denote the recovered SED by `KNNImputer`, and the red dashed curve represents the true SED of this quasar. The blue curve and shaded area are the median and 1σ SED from cell [29, 8] in SOM, where the recovered SED belongs. The lower panel shows the $\log(L_{\text{bol}})$ distribution in cell [29, 8]. The blue and red dashed line represents the median $\log(L_{\text{bol}})$ value in cell [29, 8] and the true $\log(L_{\text{bol}})$ value of this quasar. The difference $\Delta \log L_{\text{bol}} = \log(L_{\text{bol},\text{SOM}}) - \log(L_{\text{bol},\text{true}})$ is 0.02.

with S/Ns greater than 3 and interpolated at 10 features corresponding to wavelengths from 760 Å to 3.2 μm. We also obtain the X-ray emission of the quasars using the same method earlier.

If a quasar has any missing features, we recover them using the full-coverage samples with `KNNImputer` introduced in Section 4.4, i.e., the average of the 100 most similar SEDs for recovery. With the recovered SED, the

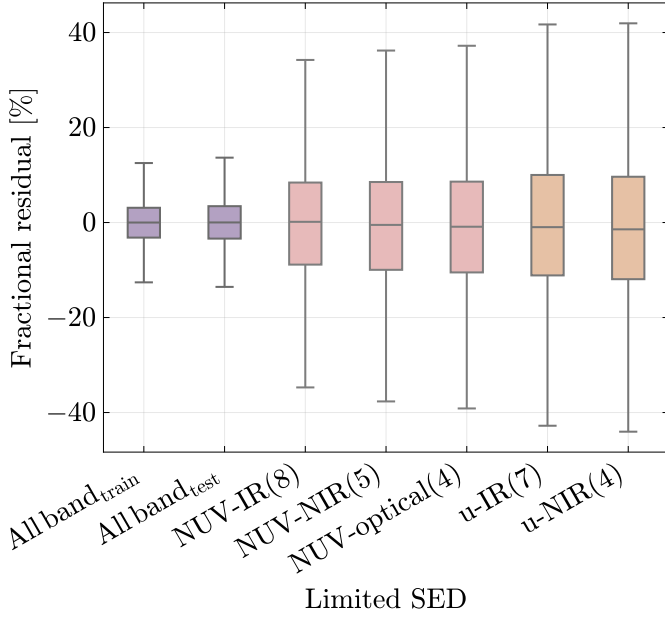


Figure 12. Fractional residuals for the limited SEDs with the SOM method. For clarity, outliers are not shown.

SOM can find the most similar subsample of the target. As we discussed in Section 4 that less information induces a larger uncertainty, here we use the modeling systematic uncertainty in the test sample with limited data from Section 4.4 as the uncertainty of predicted $\log(L_{\text{bol}})$. We publicly release bolometric luminosities for these recalculated DR16Q samples in Table 6 in Appendix A.

For quasars from 79,163 full-coverage samples and 633,373 suitable quasar samples, we compare their bolometric luminosity distribution with those from Wu & Shen (2022), who mainly used $BC = 5.15$ at 3000 \AA in Figure 13. Additionally, we bin the sample into six equally bins of $\log(L_{\text{bol, Wu}})$, and display the corresponding median values for each bin in Figure 13. Their x -axis error indicates the bin size, and their y -axis error indicates the 16th to 84th percentiles of the isotropic bolometric luminosity based on the SOM method. In summary, the median and 1σ uncertainty (i.e., half the difference between the 84th and 16th percentiles) values of $(L_{\text{bol, Wu}} - L_{\text{bol}})/L_{\text{bol}}$ are 14.8% and 43.6%, respectively.

4.6. Code Description

We make our Python code publicly available², including the fully-trained SOM model, training and test data sets, luminosity maps, and modeling systematic

² <https://github.com/ChenJiemi/QSOLbol>

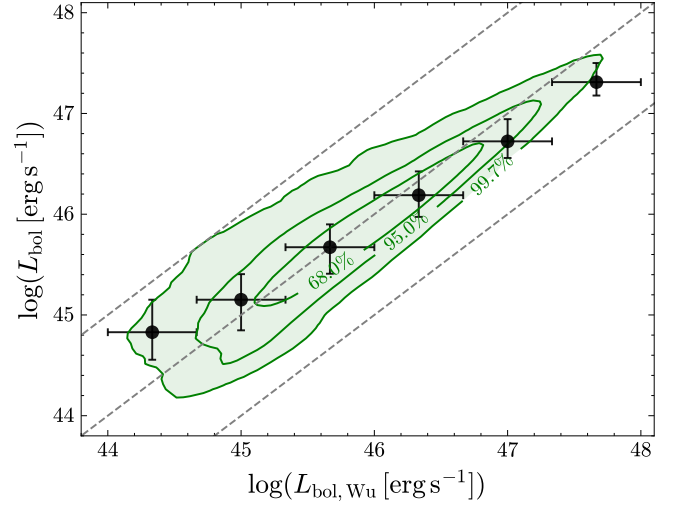


Figure 13. Comparison between $\log(L_{\text{bol}})$ from this work and $\log(L_{\text{bol, Wu}})$ from Wu & Shen (2022) for recalculated DR16Q sample. The contour level is labeled with a closed percentile. The gray dashed lines, from top to bottom, represent a line one dex higher, the one-to-one line, and a line one dex lower.

uncertainties. To compute the bolometric luminosity of a quasar, users will provide its redshift and observed-frame SED. The usage is explained by an example in the code package. The parameters of the main function `QSOLbol` are listed in Table 5. Users can modify the parameter `f_isotropy` to control the viewing angle correction from Runnoe et al. (2012a). The wavelength range of bolometric luminosity can be generated according to users' requirements, and the range of the selection should be in the range of $4 \mu\text{m}$ -10 keV.

Since our samples are small in number at the faint and bright luminosity ends, we add a scaling parameter to scale up or scale down the SEDs of the faint ($\log(L_{\text{bol}}/\text{erg s}^{-1}) < 45.13$) or bright sources ($\log(L_{\text{bol}}/\text{erg s}^{-1}) > 46.74$). We use the SOM to calculate the bolometric luminosity iteratively. This approach allows for a more accurate calculation of the bolometric luminosity for the bright and faint end sources. We add this scaling parameter as an option in the code. The function returns $\log(L_{\text{bol}})$, its corresponding uncertainty and scaling factor following the procedures in Section 4.5.

5. SUMMARY

We have developed a new method to estimate quasar isotropic bolometric luminosities. Our approach is based on a sample of 79,163 quasars in the redshift range of 0.5 to 2 from SDSS DR16Q. These quasars have multi-wavelength data spanning the wavelength range from the mid-IR to the UV (Table 6). After correcting the

Table 5. Parameters in QSOLbo1

Parameters	Type	Description
wave	array-like	Observed-frame SED wavelength in Angstrom.
mags	array-like	Observed-frame SED in AB magnitude.
mags_err	array-like	Observed-frame SED error in AB magnitude.
z	1D array-like	Redshift.
f_isotropy	bool	Whether to use 0.75 correction for viewing angle. The default is False.
wave_range	tuple	The integrated range of bolometric luminosity in Hz. The default is from $4\mu\text{m}$ to 2 keV.
scale	bool	Whether to scale the SED when the source is at faint and bright luminosity ends.

IGM absorption and host galaxy contamination, we constructed SEDs and computed their bolometric luminosities. The main results are summarized below.

1. We constructed a median SED of these quasars, with a restframe coverage from $4\mu\text{m}$ to 2 keV. The normalized SED clearly shows the diversity of quasar SEDs (see Figures 2 and 3; Section 3).
2. We computed the bolometric correction and multi-band linear regression for the quasar sample. These relations show a large scatter with σ_f about 13% to 36% (see Figure 4 and Tables 1, 2 and 3; Section 3).
3. We used an unsupervised neural network SOM to describe the SED diversity and used a fully-train SOM model to compute quasar bolometric luminosities. With full coverage SED features, i.e., 11 restframe monochromatic luminosities from $3.2\mu\text{m}$ to 2 keV, our bolometric luminosity computation is robust and efficient, with σ_f about 4.9% (see Figures 7, 9, and 10; Section 4).
4. For quasars with limited SEDs, we used KNNImputer to recover the missing features. Briefly, for a limited SED with given features, the most similar SED is found in the training set samples, and the missing features are replaced with the average of the 100 most similar SEDs. Hence, a quasar with a limited SED can also be applied in the SOM model to compute its bolometric luminosity (see Figures 11 and 12; Section 4).
5. We applied this SOM method to the SDSS DR16Q quasars and calculated their bolometric luminosities (see Figure 13; Section 4).

We have demonstrated that combining the strength of photometric surveys with the advanced machine learning tool SOM offers a pathway to overcome the challenge of calculating robust bolometric luminosities for large numbers of quasars. The accuracy of individual source bolometric luminosity can be further improved by reliable measurements of AGN host galaxies and simultaneous observations. Future deep ultraviolet facilities such as the China Space Station Telescope would prompt the quasar EUV SED study for bolometric luminosity computation and also the understanding of the quasar central engine. In future work, we will further explore the effect of the unseen EUV part of the SED, host galaxy decomposition, and non-simultaneous effects, and characterize these systematic uncertainties in the bolometric luminosity.

- 1 We thank Bernie Shiao and Yuhan Wen for the helpful
- 2 discussion in GALEX cross-matching. We thank Zhi-
- 3 wei Pan and Gaocheng Yin for their suggestions. We
- 4 acknowledge support from the National Key R&D Pro-
- 5 gram of China (2022YFF0503401) and the National Sci-
- 6 ence Foundation of China (12225301, 12322303).

Software: AstroML (VanderPlas et al. 2012), Jupyter notebooks (Perez & Granger 2007), Matplotlib (Hunter 2007), Numpy & Scipy (van der Walt et al. 2011), SomPY (Moosavi et al. 2014), SCIKIT-LEARN (Pedregosa et al. 2011).

APPENDIX

A. CATALOG FOR SDSS DR16Q

We present the multi-band photometry and bolometric luminosities of the SDSS DR16Q quasars that satisfy $z < 5$ and $\log(L_{2500}/\text{erg s}^{-1}) > 43.7$ in Table 6. The uncertainty of each quantity is also included in the catalog. This catalog includes 79,163 full-coverage quasars and 633,373 suitable quasars. SDSS and GALEX magnitudes are in the AB system. UHS, UKIDSS, VHS, and WISE magnitudes are in the Vega system.

Table 6. Multiwavelength Quasar Catalog Format

Column	Name	Description
1	R.A.	Right ascension in decimal degrees (J2000)
2	Decl.	Declination in decimal degrees (J2000)
3	Redshift	Spectroscopic redshift from SDSS DR16Q
4	X_RAY_MATCHED	X-ray matching flag
4	Chandra_FLUX	X-ray flux from Chandra (rest-frame 2 keV) in $\text{erg/s/cm}^2/\text{keV}$
5	eROSITA_FLUX	X-ray flux from eROSITA (rest-frame 2 keV) in $\text{erg/s/cm}^2/\text{keV}$
6	XMM_FLUX	X-ray flux from XMM-Newton (rest-frame 2 keV) in $\text{erg/s/cm}^2/\text{keV}$
7	GALEX_FUV_MAG	GALEX FUV magnitude
8	GALEX_NUV_MAG	GALEX NUV magnitude
9	SDSS_u_MAG	SDSS <i>u</i> -band PSF magnitude
10	SDSS_g_MAG	SDSS <i>g</i> -band PSF magnitude
11	SDSS_r_MAG	SDSS <i>r</i> -band PSF magnitude
12	SDSS_i_MAG	SDSS <i>i</i> -band PSF magnitude
13	SDSS_z_MAG	SDSS <i>z</i> -band PSF magnitude
14	UKIRT_Y_MAG	UHS and UKIDSS Y-band magnitude
15	UKIRT_J_MAG	UHS and UKIDSS J-band magnitude
16	UKIRT_H_MAG	UHS and UKIDSS H-band magnitude
17	UKIRT_K_MAG	UHS and UKIDSS K-band magnitude
18	VHS_Y_MAG	VHS Y-band magnitude
19	VHS_J_MAG	VHS J-band magnitude
20	VHS_H_MAG	VHS H-band magnitude
21	VHS_K_MAG	VHS K-band magnitude
22	WISE_W1_MAG	WISE W1-band magnitude
23	WISE_W2_MAG	WISE W2-band magnitude
24	WISE_W3_MAG	WISE W3-band magnitude
25	WISE_W4_MAG	WISE W4-band magnitude
26	logLbol	Bolometric luminosity in log for full-coverage samples
27	logLbol_SOM	Bolometric luminosity in log from SOM method
28	logLbol_Wu	Bolometric luminosity in log from Wu & Shen (2022) .

NOTE—This table is available in a machine-readable format in the online journal.

REFERENCES

- Acquaviva, V. 2016, MNRAS, 456, 1618, doi: [10.1093/mnras/stv2703](https://doi.org/10.1093/mnras/stv2703)
- Assef, R. J., Kochanek, C. S., Brodwin, M., et al. 2010, ApJ, 713, 970, doi: [10.1088/0004-637X/713/2/970](https://doi.org/10.1088/0004-637X/713/2/970)

- Auge, C., Sanders, D., Treister, E., et al. 2023, *ApJ*, 957, 19, doi: [10.3847/1538-4357/acf21a](https://doi.org/10.3847/1538-4357/acf21a)
- Ball, N. M., & Brunner, R. J. 2010, *International Journal of Modern Physics D*, 19, 1049, doi: [10.1142/S02182718100017160](https://doi.org/10.1142/S02182718100017160)
- Baron, D. 2019, arXiv e-prints, arXiv:1904.07248, doi: [10.48550/arXiv.1904.07248](https://doi.org/10.48550/arXiv.1904.07248)
- Barthel, P. D. 1989, *ApJ*, 336, 606, doi: [10.1086/167038](https://doi.org/10.1086/167038)
- Bianchi, L. 2014, *Ap&SS*, 354, 103, doi: [10.1007/s10509-014-1935-6](https://doi.org/10.1007/s10509-014-1935-6)
- Bianchi, L., Shiao, B., & Thilker, D. 2017, *ApJS*, 230, 24, doi: [10.3847/1538-4365/aa7053](https://doi.org/10.3847/1538-4365/aa7053)
- Brightman, M., Baloković, M., Ballantyne, D. R., et al. 2017, *ApJ*, 844, 10, doi: [10.3847/1538-4357/aa75c9](https://doi.org/10.3847/1538-4357/aa75c9)
- Bruursema, J., Vrba, F., Munn, J., et al. 2023, *Bulletin of the AAS*, 55
- Cai, Z.-Y., & Wang, J.-X. 2023, *Nature Astronomy*, 7, 1506, doi: [10.1038/s41550-023-02088-5](https://doi.org/10.1038/s41550-023-02088-5)
- Calistro Rivera, G., Lusso, E., Hennawi, J. F., & Hogg, D. W. 2016, *ApJ*, 833, 98, doi: [10.3847/1538-4357/833/1/98](https://doi.org/10.3847/1538-4357/833/1/98)
- Camarota, L., & Holberg, J. B. 2014, *MNRAS*, 438, 3111, doi: [10.1093/mnras/stt2422](https://doi.org/10.1093/mnras/stt2422)
- Chatfield, C., & Collins, A. J. 1980, *Principal component analysis* (Boston, MA: Springer US), 57–81, doi: [10.1007/978-1-4899-3184-9_4](https://doi.org/10.1007/978-1-4899-3184-9_4)
- Cutri, R. M., Wright, E. L., Conrow, T., et al. 2021, *VizieR Online Data Catalog: AllWISE Data Release (Cutri+ 2013)*, *VizieR On-line Data Catalog: II/328*. Originally published in: *IPAC/Caltech* (2013)
- Davidzon, I., Laigle, C., Capak, P. L., et al. 2019, arXiv e-prints, arXiv:1905.13233, <https://arxiv.org/abs/1905.13233>
- Duras, F., Bongiorno, A., Ricci, F., et al. 2020, *A&A*, 636, A73, doi: [10.1051/0004-6361/201936817](https://doi.org/10.1051/0004-6361/201936817)
- Dye, S., Lawrence, A., Read, M. A., et al. 2018, *MNRAS*, 473, 5113, doi: [10.1093/mnras/stx2622](https://doi.org/10.1093/mnras/stx2622)
- Elvis, M., Wilkes, B. J., McDowell, J. C., et al. 1994, *ApJS*, 95, 1, doi: [10.1086/192093](https://doi.org/10.1086/192093)
- Evans, I. N., Evans, J. D., Martínez-Galarza, J. R., et al. 2024, *ApJS*, 274, 22, doi: [10.3847/1538-4365/ad6319](https://doi.org/10.3847/1538-4365/ad6319)
- Faucher-Giguère, C.-A. 2020, *MNRAS*, 493, 1614, doi: [10.1093/mnras/staa302](https://doi.org/10.1093/mnras/staa302)
- Fitzpatrick, E. L. 1999, *PASP*, 111, 63, doi: [10.1086/316293](https://doi.org/10.1086/316293)
- Fukugita, M., Ichikawa, T., Gunn, J. E., et al. 1996, *AJ*, 111, 1748, doi: [10.1086/117915](https://doi.org/10.1086/117915)
- George, I. M., Turner, T. J., Yaqoob, T., et al. 2000, *ApJ*, 531, 52, doi: [10.1086/308461](https://doi.org/10.1086/308461)
- Hemmati, S., Capak, P., Masters, D., et al. 2019, *ApJ*, 877, 117, doi: [10.3847/1538-4357/ab1be5](https://doi.org/10.3847/1538-4357/ab1be5)
- HI4PI Collaboration, Ben Bekhti, N., Flöer, L., et al. 2016, *A&A*, 594, A116, doi: [10.1051/0004-6361/201629178](https://doi.org/10.1051/0004-6361/201629178)
- Hogg, D. W., Bovy, J., & Lang, D. 2010, arXiv e-prints, arXiv:1008.4686, doi: [10.48550/arXiv.1008.4686](https://doi.org/10.48550/arXiv.1008.4686)
- Hopkins, P. F., Richards, G. T., & Hernquist, L. 2007, *ApJ*, 654, 731, doi: [10.1086/509629](https://doi.org/10.1086/509629)
- Hubeny, I., Blaes, O., Krolik, J. H., & Agol, E. 2001, *ApJ*, 559, 680, doi: [10.1086/322344](https://doi.org/10.1086/322344)
- Hunter, J. D. 2007, *Computing in Science and Engineering*, 9, 90, doi: [10.1109/MCSE.2007.55](https://doi.org/10.1109/MCSE.2007.55)
- Jalan, P., Rakshit, S., Woo, J.-J., Kotilainen, J., & Stalin, C. S. 2023, *MNRAS*, 521, L11, doi: [10.1093/mnras/slado14](https://doi.org/10.1093/mnras/slado14)
- Jin, C., Ward, M., & Done, C. 2012, *MNRAS*, 425, 907, doi: [10.1111/j.1365-2966.2012.21272.x](https://doi.org/10.1111/j.1365-2966.2012.21272.x)
- Kim, D., Im, M., Kim, M., et al. 2023, *ApJ*, 954, 156, doi: [10.3847/1538-4357/aceb5e](https://doi.org/10.3847/1538-4357/aceb5e)
- Kohonen, T. 1982, *Biological Cybernetics*, 43, 59, doi: [10.1007/BF00337288](https://doi.org/10.1007/BF00337288)
- Krawczyk, C. M., Richards, G. T., Mehta, S. S., et al. 2013, *ApJS*, 206, 4, doi: [10.1088/0067-0049/206/1/4](https://doi.org/10.1088/0067-0049/206/1/4)
- La Torre, V., & Pacucci, F. 2024, arXiv e-prints, arXiv:2410.11951, doi: [10.48550/arXiv.2410.11951](https://doi.org/10.48550/arXiv.2410.11951)
- La Torre, V., Sajina, A., Goulding, A. D., et al. 2024, *AJ*, 167, 261, doi: [10.3847/1538-3881/ad3821](https://doi.org/10.3847/1538-3881/ad3821)
- Lawrence, A., Warren, S. J., Almaini, O., et al. 2007, *MNRAS*, 379, 1599, doi: [10.1111/j.1365-2966.2007.12040.x](https://doi.org/10.1111/j.1365-2966.2007.12040.x)
- Lusso, E., Comastri, A., Simmons, B. D., et al. 2012, *MNRAS*, 425, 623, doi: [10.1111/j.1365-2966.2012.21513.x](https://doi.org/10.1111/j.1365-2966.2012.21513.x)
- Lyke, B. W., Higley, A. N., McLane, J. N., et al. 2020, *ApJS*, 250, 8, doi: [10.3847/1538-4365/aba623](https://doi.org/10.3847/1538-4365/aba623)
- Lynds, R. 1971, *ApJL*, 164, L73, doi: [10.1086/180695](https://doi.org/10.1086/180695)
- Lyu, J., & Rieke, G. H. 2017, *ApJ*, 841, 76, doi: [10.3847/1538-4357/aa7051](https://doi.org/10.3847/1538-4357/aa7051)
- Marconi, A., Risaliti, G., Gilli, R., et al. 2004, *MNRAS*, 351, 169, doi: [10.1111/j.1365-2966.2004.07765.x](https://doi.org/10.1111/j.1365-2966.2004.07765.x)
- Martin, D. C., Fanson, J., Schiminovich, D., et al. 2005, *ApJL*, 619, L1, doi: [10.1086/426387](https://doi.org/10.1086/426387)
- McMahon, R. G., Banerji, M., Gonzalez, E., et al. 2013, *The Messenger*, 154, 35
- Merloni, A., Lamer, G., Liu, T., et al. 2024, *A&A*, 682, A34, doi: [10.1051/0004-6361/202347165](https://doi.org/10.1051/0004-6361/202347165)
- Moosavi, V., Packmann, S., & Vallés, I. 2014, *SOMPY: A Python Library for Self Organizing Map (SOM)*
- Morrissey, P., Conrow, T., Barlow, T. A., et al. 2007, *ApJS*, 173, 682, doi: [10.1086/520512](https://doi.org/10.1086/520512)
- Nemmen, R. S., & Brotherton, M. S. 2010, *MNRAS*, 408, 1598, doi: [10.1111/j.1365-2966.2010.17224.x](https://doi.org/10.1111/j.1365-2966.2010.17224.x)

- Novikov, I. D., & Thorne, K. S. 1973, in *Black Holes (Les Astres Occlus)*, 343–450
- Pedregosa, F., Varoquaux, G., Gramfort, A., et al. 2011, *Journal of Machine Learning Research*, 12, 2825, doi: [10.48550/arXiv.1201.0490](https://doi.org/10.48550/arXiv.1201.0490)
- Perez, F., & Granger, B. E. 2007, *Computing in Science and Engineering*, 9, 21, doi: [10.1109/MCSE.2007.53](https://doi.org/10.1109/MCSE.2007.53)
- Prochaska, J. X., Worseck, G., & O’Meara, J. M. 2009, *ApJL*, 705, L113, doi: [10.1088/0004-637X/705/2/L113](https://doi.org/10.1088/0004-637X/705/2/L113)
- Ranalli, P., Georgantopoulos, I., Corral, A., et al. 2015, *A&A*, 577, A121, doi: [10.1051/0004-6361/201425246](https://doi.org/10.1051/0004-6361/201425246)
- Ren, W., Guo, H., Shen, Y., et al. 2024, arXiv e-prints, arXiv:2406.17598, doi: [10.48550/arXiv.2406.17598](https://doi.org/10.48550/arXiv.2406.17598)
- Richards, G. T., Lacy, M., Storrie-Lombardi, L. J., et al. 2006, *ApJS*, 166, 470, doi: [10.1086/506525](https://doi.org/10.1086/506525)
- Rosario, D. J., Trakhtenbrot, B., Lutz, D., et al. 2013, *A&A*, 560, A72, doi: [10.1051/0004-6361/201322196](https://doi.org/10.1051/0004-6361/201322196)
- Runnøe, J. C., Brotherton, M. S., & Shang, Z. 2012a, *MNRAS*, 422, 478, doi: [10.1111/j.1365-2966.2012.20620.x](https://doi.org/10.1111/j.1365-2966.2012.20620.x)
- . 2012b, *MNRAS*, 426, 2677, doi: [10.1111/j.1365-2966.2012.21644.x](https://doi.org/10.1111/j.1365-2966.2012.21644.x)
- Schlafly, E. F., & Finkbeiner, D. P. 2011, *ApJ*, 737, 103, doi: [10.1088/0004-637X/737/2/103](https://doi.org/10.1088/0004-637X/737/2/103)
- Schlafly, E. F., Meisner, A. M., & Green, G. M. 2019, *ApJS*, 240, 30, doi: [10.3847/1538-4365/aafbea](https://doi.org/10.3847/1538-4365/aafbea)
- Schlegel, D. J., Finkbeiner, D. P., & Davis, M. 1998, *ApJ*, 500, 525, doi: [10.1086/305772](https://doi.org/10.1086/305772)
- Schmidt, M., & Green, R. F. 1983, *ApJ*, 269, 352, doi: [10.1086/161048](https://doi.org/10.1086/161048)
- Shakura, N. I., & Sunyaev, R. A. 1976, *MNRAS*, 175, 613, doi: [10.1093/mnras/175.3.613](https://doi.org/10.1093/mnras/175.3.613)
- Shang, Z., Brotherton, M. S., Wills, B. J., et al. 2011, *ApJS*, 196, 2, doi: [10.1088/0067-0049/196/1/2](https://doi.org/10.1088/0067-0049/196/1/2)
- Shangguan, J., Ho, L. C., Bauer, F. E., Wang, R., & Treister, E. 2020, *ApJ*, 899, 112, doi: [10.3847/1538-4357/aba8a1](https://doi.org/10.3847/1538-4357/aba8a1)
- Shen, Y., Richards, G. T., Strauss, M. A., et al. 2011, *ApJS*, 194, 45, doi: [10.1088/0067-0049/194/2/45](https://doi.org/10.1088/0067-0049/194/2/45)
- Sobolewska, M. A., Siemiginowska, A., & Życki, P. T. 2004a, *ApJ*, 608, 80, doi: [10.1086/392529](https://doi.org/10.1086/392529)
- . 2004b, *ApJ*, 617, 102, doi: [10.1086/425262](https://doi.org/10.1086/425262)
- Stalevski, M., Ricci, C., Ueda, Y., et al. 2016, *MNRAS*, 458, 2288, doi: [10.1093/mnras/stw444](https://doi.org/10.1093/mnras/stw444)
- Steffen, A. T., Strateva, I., Brandt, W. N., et al. 2006, *AJ*, 131, 2826, doi: [10.1086/503627](https://doi.org/10.1086/503627)
- Su, T., Guo, Q., Qiao, E., et al. 2025, arXiv e-prints, arXiv:2501.10793, doi: [10.48550/arXiv.2501.10793](https://doi.org/10.48550/arXiv.2501.10793)
- Trammell, G. B., Vanden Berk, D. E., Schneider, D. P., et al. 2007, *AJ*, 133, 1780, doi: [10.1086/511817](https://doi.org/10.1086/511817)
- Traulsen, I., Schwöpe, A. D., Lamer, G., et al. 2020, *A&A*, 641, A137, doi: [10.1051/0004-6361/202037706](https://doi.org/10.1051/0004-6361/202037706)
- Troyanskaya, O., Cantor, M., Sherlock, G., et al. 2001, *Bioinformatics*, 17, 520, doi: [10.1093/bioinformatics/17.6.520](https://doi.org/10.1093/bioinformatics/17.6.520)
- Ueda, Y., Akiyama, M., Ohta, K., & Miyaji, T. 2003, *ApJ*, 598, 886, doi: [10.1086/378940](https://doi.org/10.1086/378940)
- van der Walt, S., Colbert, S. C., & Varoquaux, G. 2011, *Computing in Science and Engineering*, 13, 22, doi: [10.1109/MCSE.2011.37](https://doi.org/10.1109/MCSE.2011.37)
- Vanden Berk, D. E., Richards, G. T., Bauer, A., et al. 2001, *AJ*, 122, 549, doi: [10.1086/321167](https://doi.org/10.1086/321167)
- VanderPlas, J., Connolly, A. J., Ivezi, Z., & Gray, A. 2012, in *2012 Conference on Intelligent Data Understanding*, 47–54, doi: [10.1109/CIDU.2012.6382200](https://doi.org/10.1109/CIDU.2012.6382200)
- Vasudevan, R. V., & Fabian, A. C. 2007, *MNRAS*, 381, 1235, doi: [10.1111/j.1365-2966.2007.12328.x](https://doi.org/10.1111/j.1365-2966.2007.12328.x)
- Volonteri, M., Haardt, F., & Madau, P. 2003, *ApJ*, 582, 559, doi: [10.1086/344675](https://doi.org/10.1086/344675)
- Wall, R. E., Kilic, M., Bergeron, P., & Leiphart, N. D. 2023, *MNRAS*, 523, 4067, doi: [10.1093/mnras/stad1699](https://doi.org/10.1093/mnras/stad1699)
- Wall, R. E., Kilic, M., Bergeron, P., et al. 2019, *MNRAS*, 489, 5046, doi: [10.1093/mnras/stz2506](https://doi.org/10.1093/mnras/stz2506)
- Webb, N. A., Coriat, M., Traulsen, I., et al. 2020, *A&A*, 641, A136, doi: [10.1051/0004-6361/201937353](https://doi.org/10.1051/0004-6361/201937353)
- Wright, E. L., Eisenhardt, P. R. M., Mainzer, A. K., et al. 2010, *AJ*, 140, 1868, doi: [10.1088/0004-6256/140/6/1868](https://doi.org/10.1088/0004-6256/140/6/1868)
- Wu, Q., & Shen, Y. 2022, *ApJS*, 263, 42, doi: [10.3847/1538-4365/ac9ead](https://doi.org/10.3847/1538-4365/ac9ead)
- York, D. G., Adelman, J., Anderson, Jr., J. E., et al. 2000, *AJ*, 120, 1579, doi: [10.1086/301513](https://doi.org/10.1086/301513)
- Yuan, F., & Narayan, R. 2014, *ARA&A*, 52, 529, doi: [10.1146/annurev-astro-082812-141003](https://doi.org/10.1146/annurev-astro-082812-141003)
- Yuan, H. B., Liu, X. W., & Xiang, M. S. 2013, *MNRAS*, 430, 2188, doi: [10.1093/mnras/stt039](https://doi.org/10.1093/mnras/stt039)
- Zhuang, M.-Y., Ho, L. C., & Shangguan, J. 2021, *ApJ*, 906, 38, doi: [10.3847/1538-4357/abc94d](https://doi.org/10.3847/1538-4357/abc94d)